RSC Advances

ROYAL SOCIETY OF CHEMISTRY

www.rsc.org/advances

Graphical abstract

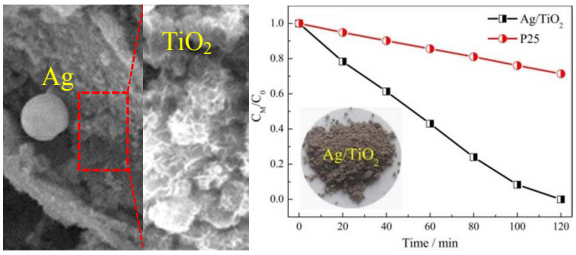

Mesoporous Ag/TiO_2 nanocomposites fabricated by dealloying/calcination show superior photocatalytic performance under visible light as well as UV irradiation.

Mesoporous Ag/TiO_2 nanocomposites with greatly enhanced photocatalytic performance towards degradation of methyl orange under visible light

Zhengfeng Zhao [a, b], Yingzi Wang[a], Jing Xu[a], Yan Wang [a, b] *

[a] School of Materials Science and Engineering, University of Jinan, No. 336, West Road of Nan Xinzhuang, Jinan 250022, PR China

[b] Shandong Provincial Key Laboratory of Preparation & Measurement of Building Materials, University of Jinan, No. 336, West Road of Nan Xinzhuang, Jinan 250022, PR China

Abstract

Ag/TiO_2 photocatalysis has received tremendous attention as a potential solution to the worldwide energy shortage and for counteracting environmental degradation. Here, the combination of dealloying with calcination has been used to fabricate mesoporous Ag/TiO_2 nanocomposites with large specific surface area of 90.18 m^2/g. In these nanocomposites, the Ag nanoparticles are well dispersed in the mesoporous anatase TiO_2 matrix with a 3 dimensional network structure. More importantly, the Ag/TiO_2 nanocomposites show greatly enhanced photocatalytic performance for the degradation of methyl orange under visible light as well as UV irradiation, compared to that of P25. The photocatalytic mechanism has been rationalized on the basis of Schottky junction, co-existence of metallic Ag, and large specific surface area. The present Ag/TiO_2 nanocomposites show great potentials for photocatalysis under solar light.

* Corresponding author. Tel: 86-531-82765473; Fax: 86-531-87974453

E-mail address: mse_wangy@ujn.edu.cn (Yan Wang).

Introduction

Electron-hole pairs can be excited from titanium dioxide (TiO_2) under light illumination. Therefore, TiO_2 is widely applied as semiconductor photocatalyst. However, the photocatalytic efficiency of TiO_2 is poor because the excited state conduction-band (CB) electrons and valence-band (VB) holes will recombine and dissipate the input energy in the form of heat or emitted light.[1] To prevent the recombination of electron-hole pairs, the approach that has generally been applied is to load the noble metal (Ag, Au, Pt, Pd, etc.) nanoclusters on the semiconductor surface.[2] In general, the noble metal nanoclusters can function as effective cocatalysts, form a Schottky junction and enhance the visible light absorption.[3]

Conventionally, the noble metal nanoparticles can be deposited onto semiconductor by deposition−precipitation or photodeposition methods.[4-8] It is well known that the size, loading and morphology of the noble metal nanoparticles on TiO_2 matrix are the important parameters for enhancing photocatalytic activity by visible light.[9, 10] However, these methods appear to be ineffective in these parameters. In order to improve the photocatalytic activity of TiO_2, several complex approaches have been used to control the size, loading and morphology of the noble metal nanoparticles. Chen et al.[10] reported the synthesis of TiO_2-supported Ag nanoclusters with excellent control of the cluster size (<5 nm) by one-pot sol–gel method. Yin et al.[11] have prepared Au/TiO_2 with high photocatalytic activity by controlling the Au nanoparticles with the size of 10 nm using the ligand-exchange method. Generally, all of these methods are always difficult to considering both the noble metal

nanoparticles and the TiO_2 matrix, any one of which will influence the photocatalytic activity. Therefore, it is highly desirable to develop novel routes to controllably fabricate noble metal-semiconductor nanocomposites with tunable compositions/microstructures and enhanced photocatalytic activity by visible light.

Among all noble metals, Ag is particularly suitable for industrial applications because it is nontoxic and of low cost relative to other noble metals. In addition, the specific surface area is another important factor to explore the photocatalytic efficiency of TiO_2. Several approaches have been extensively studied in the past decades, such as hydro- or solvothermal synthesis, sol–gel, microwave-assisted method.[12] As is known to all, the larger the specific surface area photocatalysts have, the better the photocatalytic performance they will get.[13]

Dealloying (selective corrosion) is normally utilized to fabricate nanoporous metals/alloys/nanocomposites.[14-17] Ever since Erlebacher etc.[18] reported that nanporous Au can be obtained by the dealloying method, nanporous metals have been extensively investigated such as nanoporous Cu,[14] Ag,[19] Pd[20] etc. And then nanoporous alloys have also been fabricated using the dealloying method. Nanoporous Au-Pt,[21, 22] Pd-Ni,[23] Pt-Co[24] alloys with excellent performance have been obtained by dealloying different alloy precursors. In addition, nanoporous metal/oxides have attracted wide interests. Nanoporous Cu/$(Fe,Cu)_3O_4$ composites,[25] nanoporous Ag/Fe_3O_4 nanocomposites,[26] nanoporous Ag/CeO_2 ribbons[27] have been successfully fabricated using the dealloying method. Besides, pure oxide materials could also be prepared by dealloying such as WO_3,[28] Cu_2O,[29] Fe_3O_4, Mn_3O_4, Co_3O_4.[30]

For nanocomposites like $Cu/(Fe,Cu)_3O_4$,[25] and Ag/Fe_3O_4,[26] sub-microsized metal oxides disperse in the nanoporous metal matrix. In the inverse scenario, however, no literature is available. That is, nanosized metals are well distributed in a mesoporous oxide matrix.

Here, we developed a novel strategy to synthesize Ag nanoparticles modified mesoporous anatase TiO_2 photocatalysts (Ag/TiO_2 nanocomposites) through the combination of chemical dealloying with calcination on a large scale. The photocatalytic activity of the Ag/TiO_2 nanocomposites was further evaluated by degradation of methyl orange (MO) under both visible light and UV irradiation. The nano-sized Ag decorated mesoporous TiO_2 nanocomposites show excellent photocatalytic activity towards degradation of MO, which has been rationalized based upon the high specific surface area and the formation of Schottky junction.

Experimental

The alloying ingots with a composition of $Al_{97.1}Ti_{2.9}$ or $Al_{97.4}Ti_{2.4}Ag_{0.2}$ (nominal composition, at.%) were prepared by melting pure Al, Ti and Ag metals (purity > 99.9 wt.%) in a high-frequency induction furnace. Using a single roller melt spinning instrument, the pre-alloyed ingot was remelted by high-frequency induction heating and then melt-spun onto a copper roller with a diameter of 0.35 m at a speed of 1000 revolutions per minute in a controlled argon atmosphere. The ribbons obtained were typically 2-5 mm in width, 20-50 μm in thickness and several centimeters in length.

The as-spun Al-Ti or Al-Ti-Ag ribbons were dealloyed in a 4 mol/L NaOH aqueous solution under free corrosion conditions. After dealloying for 2 h at ambient temperature, the Na-titanate or Ag/Na-titanate was obtained. Then the as-dealloyed samples were washed thoroughly with deionized water for several times, in order to remove the residual chemical substances. After drying in air, the as-dealloyed samples were immersed in a 0.1 mol/L HCl aqueous solution at ambient temperature for 2 h and then washed thoroughly with deionized water. The obtained H-titanate or Ag/AgCl/H-titanate samples were calcined under 400 ^{o}C for 1 h. Then we could obtain the mesoporous anatase TiO_2 or Ag/ TiO_2 nanocomposites. The AgCl/Ag/TiO_2 nanocomposites were prepared by re-acid treating the Ag/TiO_2 sample in the 0.1 mol/L HCl aqueous solution at ambient temperature for 2 h and then washed thoroughly with deionized water.

All products were characterized by X-ray diffraction (XRD), field emission scanning electron microscopy (FESEM) with energy dispersive spectroscopy (EDS), transmission electron microscopy (TEM) with selected area electron diffraction (SAED) and high-resolution transmission electron microscopy (HRTEM). In addition, N_2 adsorption-desorption experiments of the samples were carried out at -196 ^{o}C with a V-Sorb 2800P surface area and porosity analyzer. Brunauer-Emmett-Teller (BET) method was used to calculate the specific surface area. The pore size distribution was measured from the desorption branch of isotherm using the corrected form of Kelvin equation by the Barrett-Joyner-Halenda (BJH) method. Thermogravimetry (TG) was carried out in Ar at a heating rate of 20 ^{o}C/min on a thermal analyzer. The UV-vis

diffuse reflectance spectra (DRS) were recorded in a wavelength range of 250-800 nm to study the optical performance of the samples. The X-ray photoelectron spectroscopy (XPS) was utilized to study the chemical composition on the surface of the photocatalyst.

The photocatalytic activity of the samples was evaluated by degradation of MO aqueous solution at room temperature under visible light irradiation, because MO is a kind of chemically stable and persistent containing-nitrogen dye pollutant.[31, 32] A 300W xenon lamp with 420 nm cut-filter was used as the visible light source. The photocatalytic experiments under visible light irradiation were carried out by adding 20 mg photocatalysts (P25, Ag/TiO_2 or $AgCl/Ag/TiO_2$ composites) into 25 mL MO solution (20 mg/L). The suspension was stirred in the dark for 30 min to obtain the saturated adsorption of MO before visible light illumination. In addition, a 250 W high-voltage mercury lamp was used as the UV light source. And 5 mg photocatalysts (P25 or Ag/TiO_2 composites) were added into 25 mL MO solution under UV light irradiation. The suspension was stirred in the dark for 30 min to obtain the saturated adsorption of MO before UV light illumination.

At varied irradiation time intervals, the concentration of the MO solution was measured by monitoring the absorbance at 464 nm (the maximum absorbance wavelength of MO) using a UV-Vis spectrophotometer. The catalytic performance was evaluated by the ratio of the concentration of MO after irradiation for different time (C_M) divided by the initial concentration (C_0) (i.e., C_M/C_0).

Results and discussion

Fig. 1 shows the XRD patterns of the as obtained samples using the $Al_{97.1}Ti_{2.9}$ and $Al_{97.4}Ti_{2.4}Ag_{0.2}$ precursors. After dealloying the Al-Ti ribbons in the NaOH solution, the XRD pattern (Fig. 1(aI)) of the dealloyed samples is similar to that of $Na_2Ti_2O_4(OH)_2$ (Na-titanate), as noted elsewhere.[33, 34] The H-titanate samples were obtained by acid treating the dealloyed samples and its XRD pattern is shown in Fig. 1(aII). It is clear that a diffraction peak position shifts from 28° to 25.5° after acid treatment in the HCl solution, as marked by an arrow in Fig. 1(a). The XRD pattern of the acid treatment samples (Fig. 1(aII)) is similar to the $H_xTi_{2-x/4\gamma x/4}O_4 \cdot H_2O$ (H-titanate), here $x \approx 0.7$, γ: vacancy, which has been reported in other literature.[35, 36] The formation mechanism of the H-titanate could be elucidated by the cation-exchange mechanism.[37, 38] After calcination at 400 °C, the H-titanate obtained from the Al-Ti alloy has transformed to the anatase TiO_2 (PDF#21-1272) as shown in Fig. 1(aIII).

The $Al_{97.4}Ti_{2.4}Ag_{0.2}$ was selected as the deallying precursor for the sake of adding metallic Ag to the anatase TiO_2. The XRD patterns of various samples are shown in Fig. 1(b), which are obtained under the same treating conditions with the Al-Ti precursor. After dealloying in the NaOH solution, the XRD pattern (Fig. 1(bI)) shows that the Na-titanate and face-centered cubic (fcc) Ag phase are identified in the dealloyed samples (Ag/Na-titanate). After acid treatment in the HCl solution, the H-titanate presents in the as-treated samples, suggesting the occurrence of cation-exchange. And both the fcc Ag and AgCl phases could be identified in the as-treated samples due to the transformation of partial Ag into AgCl during the acid

treatment in the HCl solution (Fig. 1(bII)). After calcining the Ag/AgCl/H-titanate at 400 ^{o}C, only the anatase TiO_2 and fcc Ag are distinguished in the as-calcined samples (Ag/TiO_2) according to the XRD pattern (Fig. 1(bIII)). On the one hand, the anatase TiO_2 can be obtained owing to the dehydrated reaction of H-titanate during the calcination process. On the other hand, all the AgCl phase has transformed to the fcc Ag phase after calcining the Ag/AgCl/H-titanate due to the reaction between the AgCl and H_2O at high temperature. The $AgCl/Ag/TiO_2$ sample was prepared by re-acid treating the Ag/TiO_2 in the 0.1 mol/ L HCl solution and the XRD pattern is shown in Fig. 1(bIV). The fcc Ag almost transforms to the AgCl phase suggesting the high chemical activity of the Ag nanoparticles.

The FESEM image in Fig. 2(a) shows the microstructure of the Na-titanate samples, which were obtained through dealloying the Al-Ti alloy in the NaOH solution. The Na-titanate exhibits a 3 dimensional (3D) network structure, which results from the selective corrosion of the elemental Al and the complicated reaction of the released Ti with NaOH. The Na, Ti and O elements are detected from the related EDS spectrum (Fig. S2(a)), which verifies the formation of Na-titanate. It should be noted that the elemental H in Na-titanate cannot be identified by the EDS analysis. After acid treatment, the 3D network structure can still be observed in the H-titanate (Fig. 2(b)). And the Na element cannot be detected from the corresponding EDS spectrum (Fig. S2(b)), implying that the cation-exchange occurred during the acid treatment process in the HCl solution (the Na^+ ions in the Na-titanate were replaced by the H^+ ions). However, this ion exchange does not significantly change

the morphology of the samples. In addition, a large amount of H_2O is released in the calcination process as depicted in Fig. S1, suggesting the existence of H element. Fig. 2(c) presents the microstructure of the anatase TiO_2 which was obtained by calcination of the H-titanate. The anatase TiO_2 shows a 3D network structure, which is inherited from the titanate. The 3D network structure of the anatase TiO_2 is beneficial to its photocatalytic performance owing to the enhanced specific surface area. Fig. 2(d) shows the FESEM images of the Ag/AgCl/H-titanate which was prepared by dealloying and further acid treatment of the Al-Ti-Ag precursor. As shown in Fig. 2(d), the Ag/AgCl nanoparticles with sizes of 200-500 nm are distributed in the H-titanate matrix, and several particles are marked by arrows. But it is difficult to distinguish metallic Ag from AgCl. The Ag and Cl elements are detected by EDS except for Ti and O elements (Fig. S2(c)), suggesting the cation-exchange and the transformation of metallic Ag in the dilute HCl solution. The 3D network structure of the H-titanate matrix indicates the additive Ag in the precursor alloy hardly changes the dealloying process. Typically, the Ag nanoparticles grow on the surface of TiO_2 to form the Schottky junction.[39, 40] In our case, the as-prepared Ag/TiO_2 samples show the analogical microstructure. Fig. 2(e) shows the microstructure of the Ag/TiO_2 samples which were fabricated by calcination of the Ag/AgCl/H-titanate at 400 ^oC. The Ag nanoparticles with sizes of tens to hundreds of nanometers are homogeneously distributed in the anatase TiO_2 matrix (some particles are highlighted by arrows in Fig. 2(e)). A spherical Ag nanoparticle is highlighted in Fig. 2(f), and the related EDS spectrum is presented in Fig. S2(d). It is clear that the

Ag element is dominant in the EDS spectrum, confirming the existence of Ag nanoparticles in the Ag/TiO_2 nanocomposites. In addition, both Ti and O can also be identified in the EDS spectrum because the spot size for EDS is larger than the Ag nanoparticle. The anatase TiO_2 matrix shows a 3D network structure which is similar to that of the pure mesoporous anatase TiO_2 (Fig. 2(c)). Fig. 2(g) shows the typical microstructure of the AgCl/Ag/TiO_2. After re-acid treatment, the metallic Ag partially transforms to the AgCl phase which exhibits the large particles with the heterogeneous size (Fig. 2(g)). Fig. 2(h) shows the distribution of Ag and Cl elements. Obviously, the same outlines of the Ag and Cl elements indicate the existence of AgCl phase, which is in agreement with Fig. 2(g). The TiO_2 matrix (marked by the dashed box in Fig. 2(g)) still presents the 3D network structure (Fig. 2(i)), indicating the stability of the anatase TiO_2 in the HCl solution.

Fig. 3 illustrates the TEM, related SAED pattern and HRTEM images of the Ag/TiO_2 photocatalyst. Fig. 3(a) exhibits that dispersive Ag nanoparticles with diameter of about tens to hundreds of nanometers are loaded in the anatase TiO_2 matrix. The matrix presents a mesoporous structure as depicted in Fig. S3. The corresponding SAED pattern is shown in Fig. 3(a-1), which is consistent with the regular diffraction rings of the anatase TiO_2. Besides, bright diffraction spots can also be observed (marked by arrows in Fig. 3(a-1)), and correspond to the fcc Ag phase. The electron diffraction results are in good agreement with the XRD analysis in Fig. 1(bIII). As shown in the enlarged image (Fig. 3(b)), the spherical Ag nanoparticles grow in the anatase TiO_2 matrix with the 3D network structure. The lattice spacings of

0.35 and 0.24 nm determined by HRTEM (Fig. 3(c)) correspond to (101) plane of the anatase TiO_2 and (111) plane of the fcc Ag phase, respectively. Moreover, the lattice distortion marked by a square at the interface between the TiO_2 matrix and Ag nanoparticles is observed, suggesting that the Schottky junction has been achieved.

Specific surface area is an important parameter for photocatalysts. The N_2 adsorption-desorption isotherm and BJH pore size distribution curves (inset) of the Ag/TiO_2 samples are displayed in Fig. S3. The hysteresis loop in the N_2 adsorption-desorption isotherm of the Ag/TiO_2 results from the filling of the framework with 3D network structure. The adsorption–desorption isotherm can be classified as a type IV isotherm with a H3-type hysteresis loop due to the presence of mesopores, which agrees with the results of the SEM and TEM. It should be noted that the BET specific surface area of the mesoporous $AgTiO_2$ is as high as 90.18 m^2/g. In addition, the specific surface area of the present Ag/TiO_2 nanocomposites is much larger than that of P25 (52 m^2/g) in other literature.[41] The BJH pore-size distribution curve indicates that the Ag/TiO_2 photocatalysts exhibit a narrow pore-size distribution with two kinds of pore diameters of 2 ~ 5 and 5 ~ 20 nm, which confirm the hierarchically porous structure of the Ag/TiO_2 samples. The mesoporous structure supplies the efficient transport pathways for the photogenerated charge carriers, which is propitious to the photocatalytic activity.[42, 43]

The fully scanned spectrum (Fig. 4(a)) shows that Ti, O, Ag and C elements exist on the surface of the Ag/TiO_2 sample. The C 1s peak at 284.6 eV is ascribed to the adventitious carbon. No other characteristic peaks can be found, suggesting the purity

of the Ag /TiO_2 nanocomposites. The high resolution XPS spectra of Ti 2p, Ag 3d and O 1s are displayed in Fig. 4(b)–4(d) respectively. Fig. 4(b) shows the peaks at 458.75 and 464.65 eV, which correspond to the Ti $2p_{3/2}$ and Ti $2p_{1/2}$ respectively. However, the peak positions for Ti 2p in the Ag/TiO_2 photocatalysts shift to the lower binding energy than the bare TiO_2, confirming the strong interface between the metallic Ag and TiO_2.[44] The XPS peaks for Ti 2p can be further divided into different peaks by XPS peak fitting program. The peak at 458.1 eV proves the existence of the Ti^{3+} oxidation state, which is advantageous to the higher photocatalytic activity for TiO_2 under the visible light irradiation. According to the areas of Ti^{3+} and Ti^{4+} (Fig. 4(b)), the ratio of Ti^{3+} was determined to be about 28.9% in total TiO_2. The Ag 3d spectrum of the Ag/TiO_2 presents two peaks at 367.9 and 373.9 eV, which are assigned to Ag $3d_{5/2}$ and Ag $3d_{3/2}$ binding energies, respectively. The XPS peak separation of 6.0 eV between two Ag 3d states is also the characteristic of metallic Ag. The peak positions of Ag 3d shift to the lower position than the bulk Ag,[45] indicating strong interface interactions between the metallic Ag and TiO_2. The shifted peak positions of the Ti 2p and Ag 3d in Ag/TiO_2 illustrate the Schottky junction between metallic Ag and TiO_2. The O 1s peak (Fig. 4(d)) at about 530 eV is the characteristic of the lattice oxygen of TiO_2. In addition, the wide and asymmetric feature of the O1s spectrum suggests that there exist more than one oxygen component in the Ag/TiO_2 photocatalyst.[46-48] The O 1s peak can be further fitted into two peaks including lattice oxygen (O_{Ti-O} at 530.1 eV) and surface hydroxyl groups (O_{O-H} at 531.7 eV).[47]

For comparison, the photocatalytic activities of commercial P25 nanoparticles,

$AgCl/Ag/TiO_2$ and mesporous Ag/TiO_2 were evaluated by photodegradation of MO solution under visible light irradiation. The photocatalytic results under visible light irradiation are shown in Fig. 5. The MO absorbance spectra (Fig. 5(a, b and c)) present the intensity of all the MO peaks decrease with the increase of treatment time indicating all of the photocatalysts can adsorb and degrade the MO solution. And MO degradation efficiency (Fig. 5(d)) illustrates the mesporous $AgCl/Ag/TiO_2$ and Ag/TiO_2 possess stronger adsorption capacity in dark originating from the mesoporous structure and the large specific area. In order to exclude the photo bleaching, the blank test is shown in Fig. 5(d) indicating the effect of light can be neglected. Of importance, the MO solution could be completely degraded in 120 min by the mesporous Ag/TiO_2 under visible light irradiation, indicating its superior photocatalytic performance. After re-acid treating the Ag/TiO_2 in the HCl solution, the $AgCl/Ag/TiO_2$ photocatalyst exhibits the poorer photocatalytic activity than the Ag/TiO_2 because of the decrease in the amount of the Schottky junctions. But it is still higher than P25 because the doping or deposition of silver halides onto TiO_2 can further enhance the photocatalytic activity.[49] And the residual Ag nanoparticles could also enhance the photocatalytic activity of the $AgCl/Ag/TiO_2$ photocatalyst. Under the same conditions, only about 27% of MO can be eliminated in 120 min by P25, showing the worst photocatalystic activity. Besides, the Ag/TiO_2 photocatalyst exhibits the enhanced photocatalytic activity under the UV light irradiation, compared to the commercial P25, as shown in Fig. S4. Therefore, the present Ag/TiO_2 photocatalyst presents excellent catalytic activities under both visible light and UV

irradiation.

In the following, we try to clarify the reasons for the enhanced photocatalytic performance of Ag/TiO_2. Ag/TiO_2 powders are black as shown in Fig. S5(e), which can absorb the visible light in the natural environment. Fig. 6 shows the optical performance of the different photocatalysts by UV-Vis diffuse reflectance. Obviously, a sharp band edge absorption peak of P25 only appears in the UV region and almost has no response in visible light region. Compared to P25, the notable absorption covering the range of 400-600 nm in the visible-light region can be observed in the spectra of Ag/TiO_2 and $AgCl/Ag/TiO_2$ nanocomposites, which is principally due to the surface plasma resonance effect of Ag nanoparticels.[47] Of importance, the band edge absorption peaks of the prepared photocatalysts shift to the visible light region. The plots of $(F(R)E)^{1/2}$ versus the energy of absorbed light are converted from the UV−Vis DRS spectra according the Kubelka-Munk function (Fig. 6 (b)). The bandgap energy of Ag/TiO_2 estimated from the intercept of the tangent to the plot is around 2.81 eV and that of the $AgCl/Ag/TiO_2$ is about 2.98 eV, which are lower than 3.16 eV of P25. As is well known, the narrower energy gap is beneficial to absorb the visible light. The results of the optical performance indicate that the modified TiO_2 by Ag nanoparticles can harvest more photons than pure TiO_2 especially under the visible light, which is in agreement with the results of photocatalytic tests.

Fig. 7 depicts a schematic illustration of enhanced photocatalytic activity by the mesoporous Ag/TiO_2 nanocomposites. It is well known that pure TiO_2 hardly degrades the MO under visible light irradiation owing to the large energy gap. It has

been demonstrated that Ag nanoparticles in the Ag/TiO_2 and $AgCl/Ag/TiO_2$ nanocomposites result in the notable response to the visible light (Fig. 6). And the Ag nanoparticles are advantageous to capture the photon.[49, 50] As for the Ag/TiO_2 nanocomposites, the hot electrons are injected into the CB of the TiO_2 matrix via the Schottky junction between Ag and TiO_2, leaving the holes in Ag nanoparticles under the visible light irradiation[51] (enlarged section in Fig. 7(a)). And the photogenerated charges would decompose the MO molecule. Under the UV light irradiation, the Ag nanoparticles serve as the scanvenging centers for causing photogenerated electron and hole pair separation (Fig. 7(b)). The excited electrons under UV spectrum can be transferred from the CB of TiO_2 to the metallic Ag by the Schottky junction (enlarged section in Fig. 7(b)), resulting in the improved photocatalytic activity[2]. In our experiment, the fcc Ag nanoparticles are distributed in the mesoporous anatase TiO_2 matrix with a 3D network structure. This unique microstructure could be used to improve the quantity of the Schottky junction and thus increase the electron transfer pathways with a certain amount of Ag content. After re-acid treating the mesoporous Ag/TiO_2 in HCl solution, almost all of the Schottky junctions between Ag and TiO_2 are damaged resulting in the decrease of the electron transfer pathways. In addition, the nansized Ag almost entirely transformed to the AgCl which cannot excite carriers under the visible light irradiation. However, the AgCl phase would be partially reduced to metallic Ag during the photodegradation process as a result of photo-instability of AgCl.[50] So the $AgCl/Ag/TiO_2$ samples present better photocatalytic performance than P25 in visible light region, but the activity is lower

than the Ag/TiO_2 photocatalyst owing to the decreasing electron transfer pathways between Ag and TiO_2.

Summary and conclusions

Novel Ag/TiO_2 nanocomposites can be fabricated through a new strategy which combines chemical dealloying/acid treatment with calcination. The dealloying of the ternary Al-Ti-Ag precursor leads to the formation of Ag/Na-titanate, and the further acid treatment gives rise to the formation of Ag/AgCl/H-titanate through the cation-exhange and chloration. The calcination of Ag/AgCl/H-titanate results in the formation of Ag/TiO_2 nanocomposites which are composed of Ag nanoparticles well distributed in the mesoporous anatase TiO_2 matrix. Compared to the commercial P25, the introduction of Ag nanoparticles can greatly enhance the photocatalytic activity of the Ag/TiO_2 nanocomposites under both visible and UV light irradiation. The enhanced photocatalytic activity of Ag/TiO_2 is attributed to the synergistic contribution of the Schottky junction between Ag and TiO_2, the surface plasma resonance effect of metallic Ag nanoparticles and the large specific surface area (90.18 m^2/g) originating from the mesoporous structure. Our strategy will provide a novel route to synthesize noble metal (Ag, Au, Pt, etc.)/oxide nanocomposites with enhanced functional properties. Moreover, the loading amount of noble metal in thesenanocomposites can be adjusted through facilely changing the composition of ternary precursor alloys (for example, the Ag/Ti ratio in the Al-Ti-Ag precursor). In

addition, the present fabrication strategy can be facilely scaled up (Fig. S5), which is crucial for the commercialization of photocatalysts.

Acknowledgements

The authors acknowledge financial support from the National Natural Science Foundation of China (No. 51171072), and Excellent Middle-age and Young Scientists Research Award Foundation of Shandong Province (No. BS2012CL002), and the international cooperation training project of excellent young and middle-aged teachers of Shandong Province.

References

1 H. Tong, S. Ouyang, Y. Bi, N. Umezawa, M. Oshikiri and J. Ye, *Adv. Mater.,* 2012, **24**, 229-251.

2 S. T. Kochuveedu, Y. H. Jang and D. H. Kim, *Chem. Soc. Rev.,* 2013,42, 8467-8493.

3 Y. Qu and X. Duan, *Chem. Soc. Rev.,* 2013, **42**, 2568-2580.

4 M. Murdoch, G. I. N. Waterhouse, M. A. Nadeem, J. B. Metson, M. A. Keane, R. F. Howe, J. Llorca and H. Idriss, *Nat. Chem.,* 2011, **3**, 489-492.

5 S. H. Nam, H. Shim, Y. Kim, M. A. Dar, J. G. Kim, and W. B. Kim, *ACS Appl. Mater. Interfaces,* 2010, **2**, 2046-2052.

6 W. Zhou, G. Du, P. Hu, G. Li, D. Wang, H. Liu, J. Wang, R. I. Boughton, D. Liu and H. Jiang, *J. Mater. Chem.,* 2011, **21**, 7937-7945.

7 V. Jovic, W. T. Chen, D. Sun-Waterhouse, M. G. Blackford, H. Idriss, and G. I. N. Waterhouse, *J. Catal.,* 2013, **305**, 307-317.

8 Q. Lu, Z. Lu, Y. Lu, L. Lv, Y. Ning, H. Yu, Y. Hou, and Y. Yin, *Nano Lett.,* 2013, **13**, 5698-5702.

9 D. Wu and M. Long, *Water Sci Technol.* 2012, **65**, 1027-1032.

10 H. Zhang, X. Li and G. Chen, *J. Mater. Chem.,* 2009, **19**, 8223-8231.

11 D. Ding, K. Liu, S. He, C. Gao and Y. Yin, *Nano Lett.,* 2014, **14**, 6731-6736.

12 T. Fröschl, U. Hörmann, P. Kubiak, G. Kucêrová, M. Pfanzelt, C. K. Weiss, R. J. Behm, N. Hüsing, U. Kaiser, K. Landfester and M. Wohlfahrt-Mehrens, *Chem. Soc. Rev.,* 2012, **41**, 5313-5360.

13 Z. Xiong and X. S. Zhao, *J. Mater. Chem. A*, 2013, **1**, 7738-7744.

14 Z. Qi, C. Zhao, X. Wang, J. Lin, W. Shao, Z. Zhang and X. Bian, *J. Phys. Chem. C,* 2009, **113**, 6694-6698.

15 H. Ji, J. Frenzel, Z. Qi, X. Wang, C. Zhao, Z. Zhang and G. Eggeler, *CrystEngComm,* 2010, **12**, 4059-4062.

16 Z. Qi, H. Geng, X. Wang, C. Zhao, H. Ji, C. Zhang, J. Xu and Z. Zhang, *J. Power Sources,* 2011, **196**, 5823-5828.

17 Z. Zhang, C. Zhang, J. Sun, T. Kou, Q. Bai, Y. Wang and Y. Ding, *J. Mater. Chem. A*, 2013, **1**, 3620-3628.

18 J. Erlebacher, M. Aziz, A. Karma, N. Dimitrov and K. Sieradzki, *Nature,* 2001, **410**, 450-453.

19 X. Wang, Z. Qi, C. Zhao, W. Wang, and Z. Zhang, *J. Phys. Chem. C,* 2009, **113**, 13139-13150.

20 C. Zhang, H. Ji, J. Sun, T. Kou, Z. Zhang, *Mater. Lett.*, 2013, **92**, 369-371.

21 H. Jin, X. Wang, S. Parida, K. Wang, M. Seo, J. Weissmüller, *Nano Lett.,* 2010, **10**, 187-194.

22 J. Xu, C. Zhang, X. Wang, H. Ji, C. Zhao, Y. Wang and Z. Zhang, *Green Chem.,* 2011,**13**, 1914-1922.

23 C. Du, M. Chen, W. Wang, and G. Yin, *ACS Appl. Mater. Interfaces,* 2011, **3**, 105-109.

24 L. Liu, E. Pippel, R. Scholz and U. Gösele, *Nano Lett.,* 2009, **9**, 4352-4358.

25 Z. Qi, Y. Gong, C. Zhang, J. Xu, X. Wang, C. Zhao, H. Ji and Z. Zhang, *J. Mater.*

Chem., 2011, **21**, 9716-9724.

26 C. Zhang, X. Wang, J. Sun, T. Kou and Z. Zhang, *CrystEngComm*, 2013,**15**, 3965-3973.

27 G. Li, F. Lu, X. Wei, X. Song, Z. Sun, Z. Yang and S. Yang, *J. Mater. Chem. A*, 2013, **1**, 4974-4981.

28 Z. Liu, T. Yamazaki, Y. Shen, D. Meng, T. Kikuta, N. Nakatani, and T. Kawabata, *J. Phys. Chem. C*, 2008, **112**, 1391-1395.

29 C. Dong, M. Zhong, T. Huang, M. Ma, D. Wortmann, M. Brajdic and I. Kelbassa, *ACS Appl. Mater. Interfaces*, 2011, **3**, 4332-4338.

30 C. Xu, R. Wang, Y. Zhang and Y. Ding, *Nanoscale*, 2010, **2**, 906-909.

31 T. Kou, C. Jin, C. Zhang, J. Sun and Z. Zhang. *RSC Adv.,* 2012, **2**, 12636–12643.

32 Z. He, W. Que and Y. He, *RSC Adv.,* 2014, **4**, 3332-3339.

33 D. Bavykin, V. Parmon, A. Lapkin and F. Walsh, *J. Mater. Chem.,* 2004, **14**, 3370-3377.

34 J. Yang, Z. Jin, X. Wang, W. Li, J. Zhang, S. Zhang, X. Guo and Z. Zhang, *Dalton Trans.,* 2003, 3898-3901.

35 F. Wu, Z. Wang, X. Li and H. Guo, *J. Mater. Chem.,* 2011, **21**, 12675-12681.

36 R. Ma, Y. Bando and T. Sasaki, *Chem. Phys. Lett.,* 2003, **380**, 577-582.

37 R. Ma, T. Sasaki and Y. Bando, *Chem. Commun.,* 2005, 948-950.

38 D. Yang, Z. Zheng, H. Liu, H. Zhu, X. Ke, Y. Xu, D. Wu and Y. Sun, *J. Phys. Chem. C,* 2008, **112**,16275-16280.

39 C. Gomes Silva, R. Juarez, T. Marino, R. Molinari and H. Garcia, *J. Am. Chem.*

Soc., 2011, **133**, 595-602.

40 C. Nijhuis, W. Reus and G. Whitesides, *J. Am. Chem. Soc.*, 2009, **131**, 17814-17827.

41 G. Schubert, T. Bánsági, and F. Solymosi, *J. Phys. Chem. C*, 2013, **117**, 22797-22804.

42 J. Low, J. Yu, Q. Li and B. Cheng, *Phys. Chem. Chem. Phys.,* 2014, **16**, 1111-1120.

43 S. K. Choi, S. Kim, S. K. Lim and H. Park, *J. Phys. Chem. C*, 2010, 114, 16475-16480.

44 C. Su, L. Liu, M. Zhang, Y. Zhang and C. Shao, *CrystEngComm,* 2012, **14**, 3989-3999.

45 H. W. Chen, Y. Ku and Y. L. Kuo, *Chem. Eng. Technol.,* 2007, **30**, 1242-1247.

46 T. Wang , X. Yan, S. Zhao, B. Lin, C. Xue, G. Yang, S. Ding, B. Yang, C. Ma, G. Yang and G. Yang, *J. Mater. Chem. A,* 2014, **2**, 15611-15619.

47 H. Zhang, G. Wang, D. Chen, X. Lv and J. H. Li, *Chem. Mater.,* 2008, **20**, 6543-6549.

48 Y. Zhang, J. Li and H. Hu, *Appl. Catal., B,* 2012, **123-124**, 18-26.

49 N. K. Shrestha, M. Yang, I. Paramasivam and P. Schmuki, *Semicond. Sci. Technol.,* 2011, **26**, 092002.

50 M. Niraula, S. Adhikari, D. Y. Lee, E. Kim, S. J. Yoon, S. K. Dhungel, W. Lee, N. K. Shrestha, S. Han, *Chem. Phys. Lett.,* 2014, **593**, 193-197.

51 C. Gomes Silva, R. Juarez, T. Marino, R. Molinari and H. Garcia, *J. Am. Chem.*

Soc., 2011, **133**, 595-602.

Figure captions

Fig. 1 XRD patterns of the obtained samples using different precursors of (a) $Al_{97.1}Ti_{2.9}$ or (b) $Al_{97.4}Ti_{2.4}Ag_{0.2}$. (I) the as-dealloyed samples, (II) the acid treatment samples, (III) the as-calcined samples, (IV) the re-acid treatment samples.

Fig. 2 FESEM images of (a) Na-titanate, (b) H-titanate, (c) the anatase TiO_2, (d) Ag/AgCl/H-titanate, (e and f) Ag/TiO_2 and (g, h and i) $AgCl/Ag/TiO_2$.

Fig. 3 (a and b) TEM images of the Ag/TiO_2 photocatalyst, (a-1) corrosponding SAED pattern and (c) HRTEM image.

Fig. 4 XPS spectra of the Ag/TiO_2 sample: (a) survey; (b) Ti 2p; (c) Ag 3d; (d) O 1s.

Fig. 5 (a-c) UV-vis absorption spectra of MO solution under different visible light irradiation time in presence of (a) Ag/TiO_2, (b) $AgCl/Ag/TiO_2$, and (c) P25. (d) Comparison of photocatalytic performance of different photocatalysts.

Fig. 6 (a) UV-Vis diffuse reflectance absorption spectra (DRS) of diferent photocatalysts and (b) plots transformed according to the Kubelka-Munk function versus energy of light for the photocatalysts.

Fig. 7 Proposed photocatalytic schematic illustration of the Ag/TiO_2 photocatalyst under (a) visible and (b) UV light irradiation. CB: conduction-band; VB: valence-band.

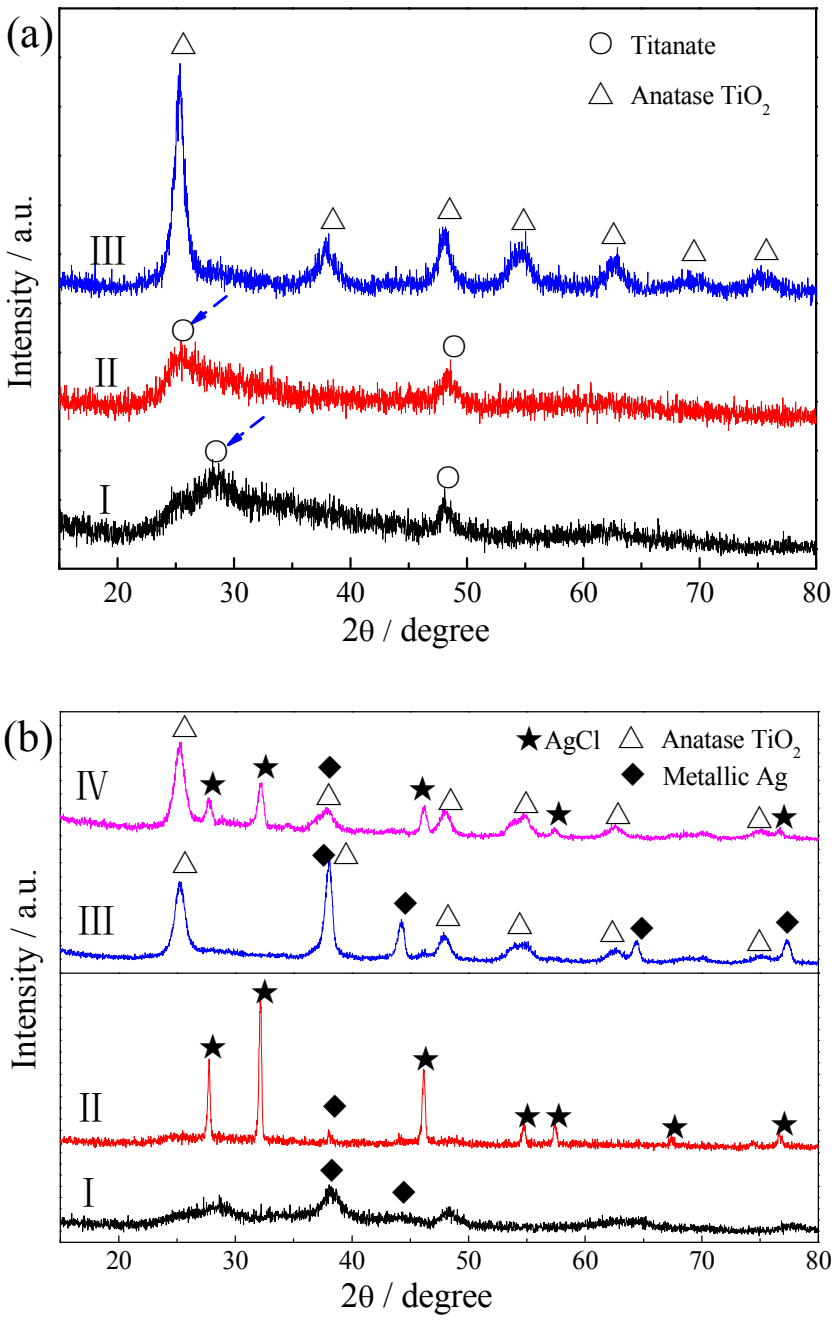

Fig. 1

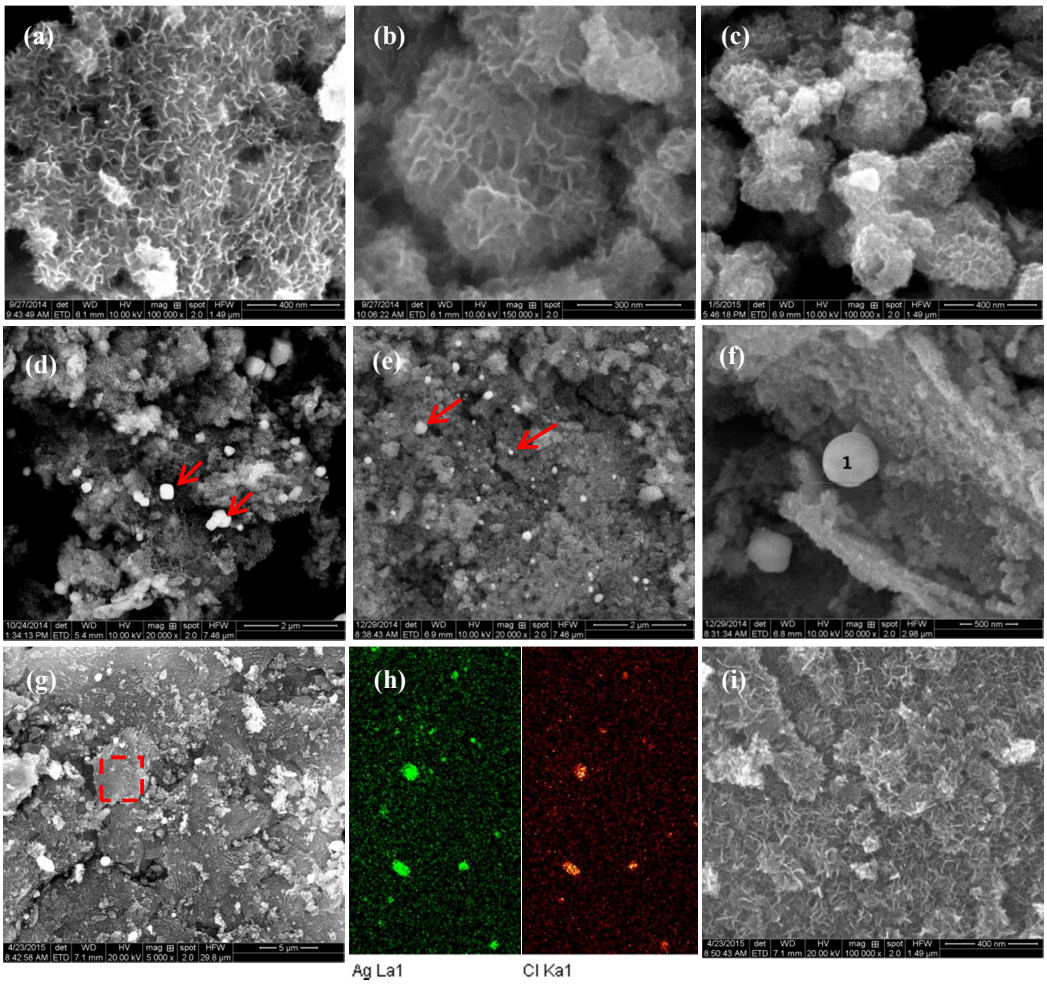

Fig. 2

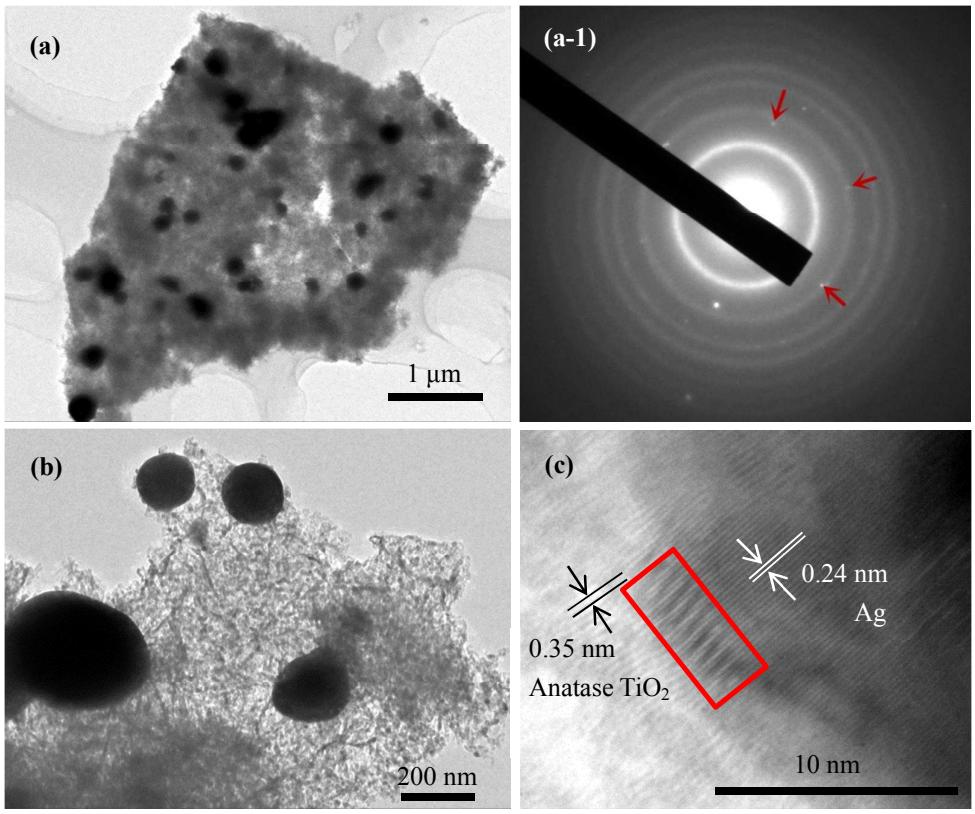

Fig. 3

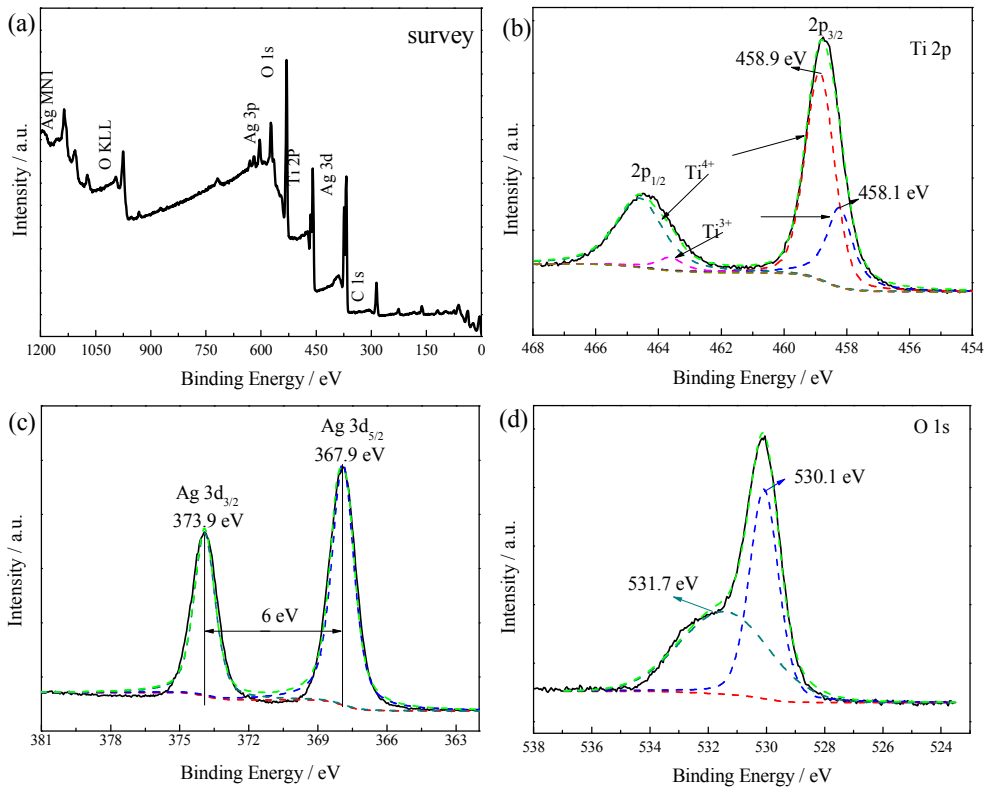

Fig. 4

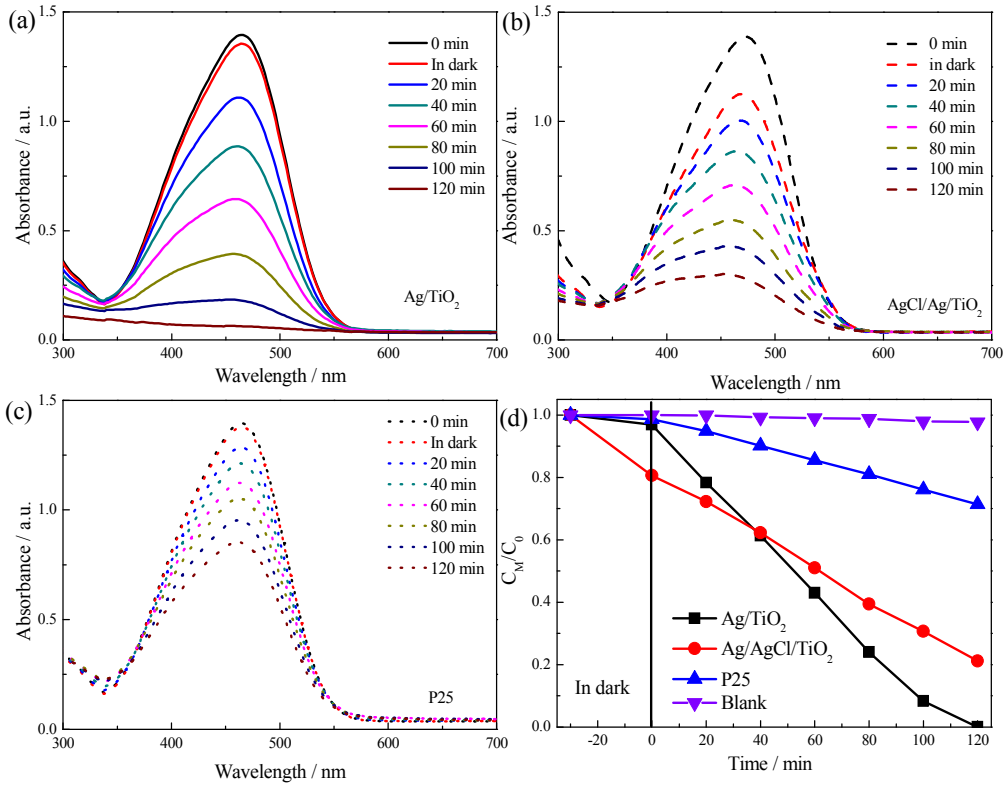

Fig. 5

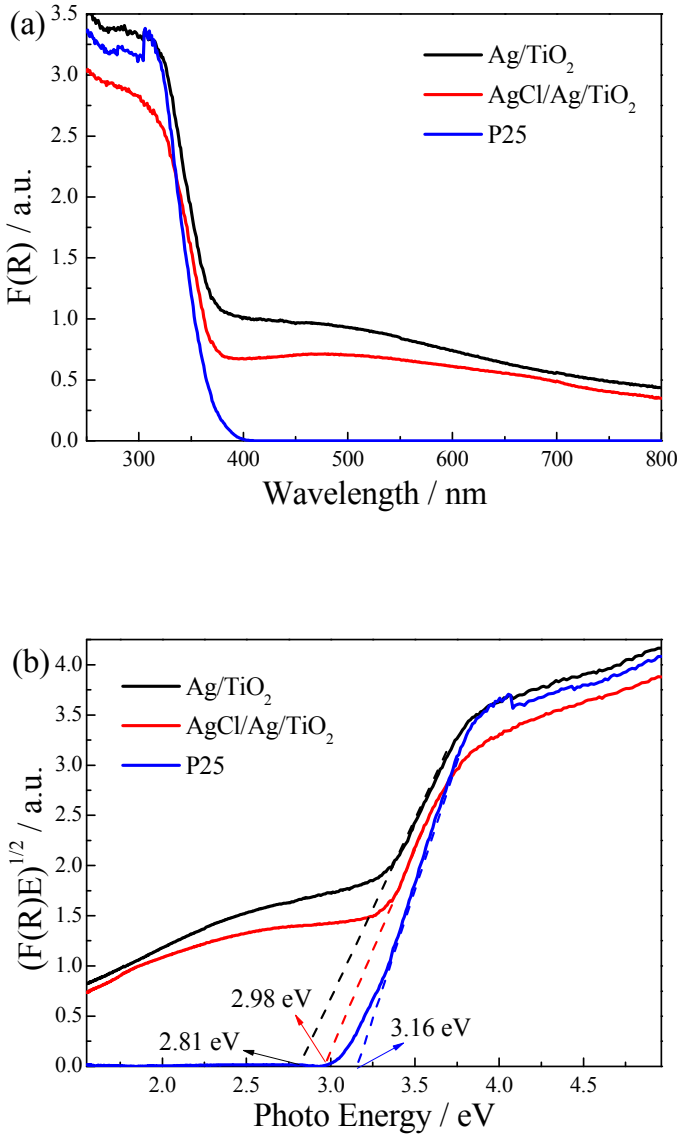

Fig. 6

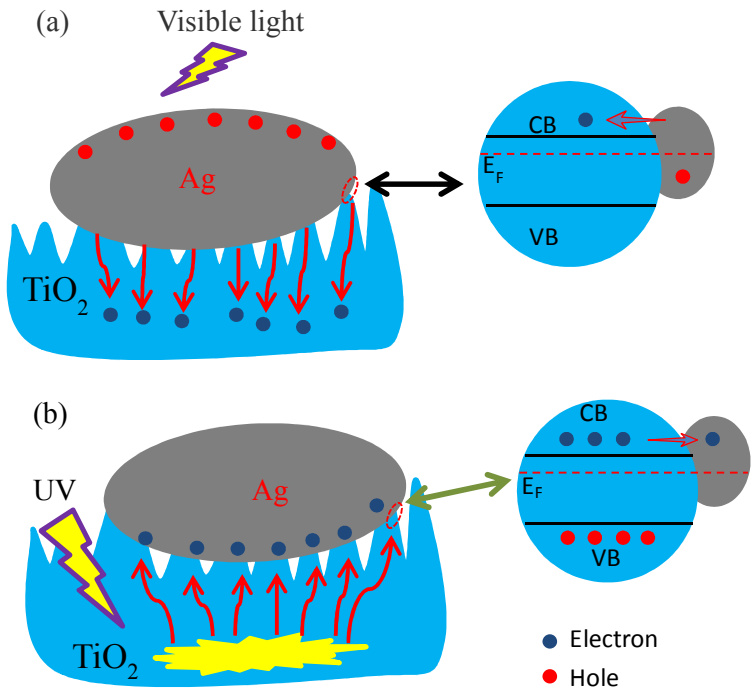

Fig. 7